ACS APPLIED MATERIALS & INTERFACES

www.acsami.org
Research Article

Engineering Triphasic Nanocomposite Coatings on Pretreated Mg Substrates for Biomedical Applications

Xijuan Chai,[#] Jiajia Lin,[#] Changlu Xu, Dongwei Sun, and Huinan Hannah Liu*

Cite This: ACS Appl. Mater. Interfaces 2024, 16, 54716−54730
Read Online

ACCESS | Metrics & More | Article Recommendations

ABSTRACT: Biodegradable polymer-based nanocomposite coatings provide multiple advantages to modulate the corrosion resistance and cytocompatibility of magnesium (Mg) alloys for biomedical applications. Biodegradable poly(glycerol sebacate) (PGS) is a promising candidate used for medical implant applications. In this study, we synthesized a new PGS nanocomposite system consisting of hydroxyapatite (HA) and magnesium oxide (MgO) nanoparticles and developed a spray coating process to produce the PGS nanocomposite layer on pretreated Mg substrates, which improved the coating adhesion at the interface and their cytocompatibility with bone marrow derived mesenchymal stem cells (BMSCs). Prior to the spray coating process of polymer-based nanocomposites, the Mg substrates were pretreated in alkaline solutions to enhance the interfacial adhesion strength of the polymer-based nanocomposite coatings. The addition of HA and MgO nanoparticles (nHA and nMgO) to the PGS matrix, as well as the alkaline pretreatment of the Mg substrates, significantly enhanced the interfacial adhesion strength when compared with the PGS coating on the nontreated Mg control. The average BMSC adhesion densities were higher on the PGS/nHA/nMgO coated Mg than the noncoated Mg controls under direct contact conditions. Moreover, the addition of nHA and nMgO to the PGS matrix and coating the nanocomposite onto Mg substrates increased the average BMSC adhesion density when compared with the PGS/nHA/nMgO coated titanium (Ti) and PGS coated Mg controls under direct contact. Therefore, the spray coating process of PGS/nHA/nMgO nanocomposites on Mg substrates or other biodegradable metal substrates could provide a promising surface treatment strategy for biodegradable implant applications.

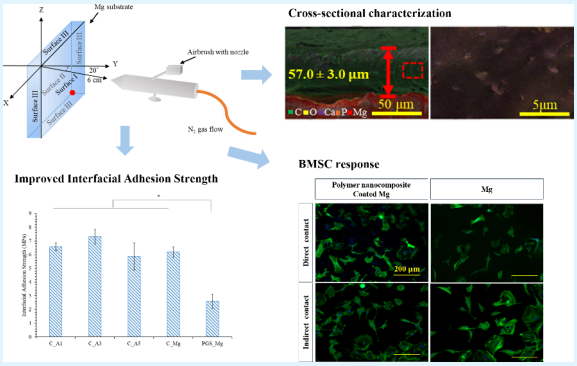

KEYWORDS: *triphasic nanocomposite coatings, magnesium (Mg) alloys, spray coating, biodegradable polymer, poly(glycerol sebacate) (PGS), hydroxyapatite (HA), magnesium oxide (MgO), cytocompatibility with BMSCs*

1. INTRODUCTION

Magnesium (Mg) alloys are promising novel biodegradable materials for medical implants because of their attractive properties, i.e., similar density and mechanical properties to those of natural cortical bone.[1−3] The biodegradability of Mg inside the body could eliminate the need of secondary surgeries for implant removal.[4,5] Moreover, Mg ions are the fourth most abundant cations in the human body and are largely stored in bone tissue.[6−8] However, the rapid degradation of Mg implants still remains as one of the key challenges, limiting their clinical translation for broad implant applications.[9,10] The presence of physiological ions and proteins could accelerate the degradation of Mg, causing the implants to lose their mechanical and structural integrity before the complete bone healing.[11−14] Polymer or polymer-based composite coatings on Mg are potential solutions to reduce the degradation rate of Mg.[3,14−16] Previous studies have found that four polymer coatings, i.e., poly(L-lactic acid) (PLLA), poly(lactic-*co*-glycolic acid) [PLGA (90:10)], PLGA (50:50), and polycaprolactone (PCL) coatings, reduced the degradation rate of Mg according to the results of electrochemical testing and human umbilical vein endothelial cell (HUVEC) culture in vitro. Additionally, the PLGA (50:50) coating improved the adhesion and spreading of HUVECs the most among the four polymer coatings.[14] Moreover, their corresponding nanocomposite coatings with nanophase hydroxyapatite (nHA), i.e., nHA/PLLA, nHA/PLGA, and nHA/PCL, significantly reduced the degradation of Mg during immersion in r-SBF, and the nHA/PCL coating showed the best overall performance in reducing the Mg degradation and improving bone marrow derived mesenchymal stem cell

Received: August 15, 2024
Revised: September 11, 2024
Accepted: September 11, 2024
Published: September 30, 2024

(BMSC) adhesion.[3] However, all these polymers are less desirable because they degrade by bulk erosion, which could produce micro- or macropores and cracks in the coatings at the early stage of the degradation process, thus allowing the diffusion of physiological solutions to the Mg substrate.[17] Alternatively, Surmeneva et al. reported[18] that parylene C coatings improved the corrosion resistance of magnesium alloys (AZ31, WE43, and AZ91) as beneficial barrier coatings because of the surface hydrophobicity and low water permeability of parylene C. Parylene C is bioinert and biocompatible, but it is unfavorable for cell adhesion and tissue engineering applications. Parylene C can degrade and oxidize when aged in vivo,[19] which could lead to embrittlement and crack formation.

In contrast, poly(glycerol sebacate) (PGS) degrades by surface erosion, which could be a better coating material for maintaining an intact residual layer during the degradation of the outer layers, impeding the diffusion of water molecules into the underlying Mg substrates and minimizing the degradation rate of Mg substrates.[17] Poly(glycerol sebacate) (PGS) is synthesized by polycondensing glycerol and sebacic acid, generating a viscous prepolymer that can be further cross-linked to form the polymer.[20] Glycerol is the basis of lipid components in the body and was approved by the US Food and Drug Administration (FDA) for usage as humectant in food.[21,22] Sebacic acid is an intermediate product in the natural metabolic process of fatty acids in the body. PGS has been shown to be biocompatible when implanted into rabbit corneas and subcutaneously into rats.[23] PGS is a bioresorbable polymer that degrades by surface erosion. Moreover, the moderate hydrophilicity of PGS can improve cell proliferation and adhesion.[24] PGS has been studied in vitro and in vivo for soft tissue engineering applications in the fields of cardiac muscle, blood vessels, and cartilage, where tissue responses indicated that PGS was biocompatible.[23,25−27] It has been reported that PGS sustained an osteoblastic phenotype attachment and proliferation in vitro when compared with the initial seeding density, which was promising for bone tissue engineering applications.[28] Please note that the PGS was serial soaked in 75%, 50%, and 30% ethanol solutions, each for 30 min, followed by phosphate buffered saline (PBS) for 1 h, and then left overnight in culture media before cell seeding.

In addition, hydroxyapatite [HA; $Ca_{10}(PO_4)_6(OH)_2$] is the predominant mineral component in natural bone and has excellent osteoconductive properties.[29−31] HA nanoparticles (nHA) are considered an attractive bioactive material because they could further promote osteoblast adhesion and proliferation with their larger surface-to-volume ratio.[31] The addition of HA nanoparticles into a polymer matrix can serve as a reinforcing phase and modify the mechanical properties of the polymer. The increase of nHA incorporation can enhance the modulus and strength of PGS because the presence of stiff hydroxyl groups can prevent C−O bending.[32,33] Moreover, nHA can tune the hydrophilicity of PGS because of the polar hydroxyl groups on its surface. MgO has attracted great attention because it can provide promising biological properties that are beneficial for bone repair.[34] MgO has been used as an oral supplement to improve bone mineral density in humans.[35] Specifically, MgO has shown stimulating effects on bone healing and regeneration in rat tibia as an implantable paste.[36] MgO nanoparticles (nMgO) exhibited antibacterial properties against both Gram-negative and Gram-positive bacteria in vitro, which is promising for reducing implant infections.[34,37−39] Therefore, HA and MgO nanoparticles could be integrated into the PGS matrix to achieve desirable bioactivity for biomedical implant applications.[40−44]

However, coating polymers directly onto nontreated Mg substrates through physical interactions often leads to weak interfacial adhesion strength to the substrates.[45] To enhance the osteogenic capacity of PGS, we proposed to incorporate bioactive ceramic nanoparticles into the cross-linked PGS network. Furthermore, surface pretreatment of Mg substrates prior to applying polymer-based coatings could also improve the interfacial adhesion strength.[3] Chen et al. found that glycerol and sebacic acid are not fully cross-linked during the curing process for PGS at the temperature of 120 °C for either 2 or 3 days, and the product still contains ester groups, excess alcohol groups, and carboxylic acid groups.[46] Therefore, we hypothesized that the functional groups of the PGS coating could react with the hydroxyl groups on the surface of Mg if the Mg substrates are pretreated with alkaline solutions to improve the interfacial adhesion strength between the polymer-based coating and Mg substrate.[47,48]

Previous studies showed that alkaline pretreatment of Mg substrates could generate a layer of $Mg(OH)_2$ that contains hydroxyl groups.[45,49,50] The $Mg(OH)_2$ layer also exhibited good interfacial adhesion strength to the Mg substrate and served as a transient protection layer in physiological solutions.[3,51,52] Therefore, the $Mg(OH)_2$ layer formed on the Mg substrate by alkaline pretreatment could improve the interfacial adhesion strength between the PGS coating and Mg substrate and reduce the corrosion rate of Mg. However, few works have systematically reported the effects of alkaline treatment parameters on the interfacial adhesion strength between the polymer-based coating and Mg substrate.

The objective of this study was to investigate the effects of alkaline pretreatment on the interfacial adhesion strength of polymer-based coatings and evaluate degradation properties and cytocompatibility of the polymer-based nanocomposite coatings on Mg substrates produced via a spray coating method. A composition of 30 wt % nanoparticles and 70 wt % PGS was used because this ceramic/polymer ratio for the nHA/nMgO/PLGA nanocomposite showed promising mechanical and biological properties in our previous studies.[43,53,54] The synergic effects of the triphasic nanocomposite consisting of nHA, nMgO, and PGS on alkaline pretreated Mg substrates have not been extensively explored for biomedical applications. In this study, it is hypothesized that nHA/nMgO/PGS coatings sprayed onto alkaline pretreated Mg substrates would improve the interfacial adhesion strength and cytocompatibility with BMSCs in vitro.

2. MATERIALS AND METHODS

2.1. Preparing Mg Substrates and the Surface Prior to the Coating Process. Biodegradable Mg-based bars (97% Mg, 3% Al, 1 mm thick; MiniScience, catalog no. MGFLAT) were cut into 10 × 10 mm squares and used as the substrates. The Mg bar was used to serve as a model substrate in this study because the main objective of this study focuses on spray coating of nanocomposite layers on a model Mg alloy substrate in combination with a pretreatment method. The addition of 3% Al is used by the commercial vendor for sacrificial anodes and is not intended to improve the corrosion properties. However, the coating process developed in this study is transferable to other Mg alloys, such as AZ31, AZ91, and WE43 alloys. All surface areas of the Mg squares, i.e., both the front surface (surface I), the back surface (surface II), and the four side surfaces (surface III), as shown in Figure 1, were ground with 600, 800, and 1200 grit silicon

https://doi.org/10.1021/acsami.4c13811
ACS Appl. Mater. Interfaces 2024, 16, 54716−54730

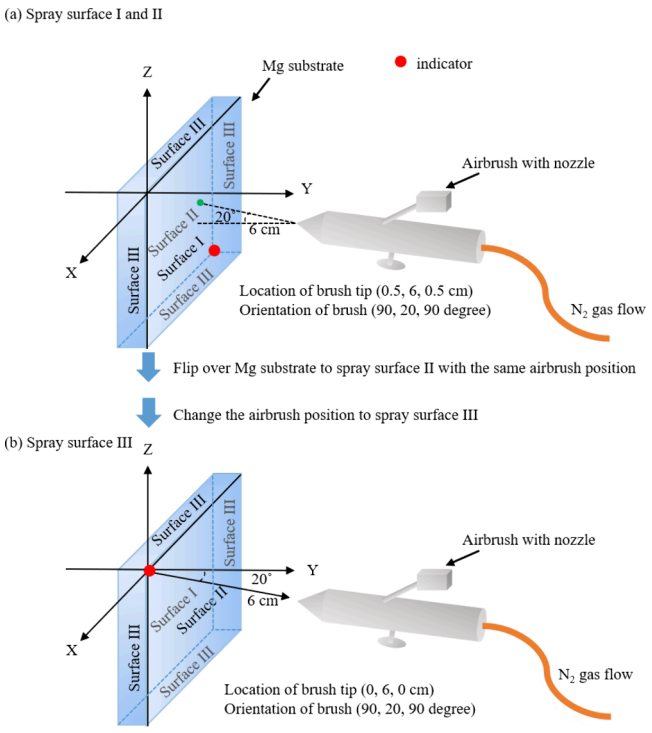

Figure 1. Spray coating process for polymer-based nanocomposites and polymer controls on Mg substrates.

carbide paper (SiC; Ted Pella) in 100% ethanol (EtOH; Koptec) to remove the oxide layers, and they were ultrasonically cleaned in acetone (Sigma-Aldrich) and ethanol, respectively, for 30 min each prior to spray coating. The polished Mg substrate was used as a degradable control, and a Ti substrate was used as a nondegradable control in this study.

The alkaline pretreatment was performed by immersing the polished Mg substrates into 1, 3, and 5 M NaOH (STREM Chemicals) solutions at 80 °C for 2 h separately and drying them in air at 60 °C for 1 h. The alkaline pretreated samples were cleaned with deionized (DI) water (Millipore Milli-Q Biocel System) for 5 min and dried at 60 °C for 30 min. The Mg samples pretreated at concentrations of 1, 3, and 5 M NaOH are referred to as A1, A3, and A5, respectively; the prefix "A" represents "alkaline treated", and the suffixes "1", "3", and "5" represent "1 M", "3 M", and "5 M", respectively. A0 refers to the polished Mg sample without alkaline treatment. All samples were kept in vacuum until used for further experiments.

2.2. Depositing Polymer-Based Nanocomposites on Mg Substrates via Spray Coating. The nHA was prepared by a wet chemistry precipitation method, as described previously.[55] Oligo(glycerol sebacate) (OGS) is the prepolymer of the biodegradable poly(glycerol sebacate) (PGS). To prepare theprepolymer suspension for spray coating, 0.6 g of OGS (Regenerez RG-100, Secant Medical, Inc., Telford, PA, US) was dissolved in 2 mL of pure ethanol to produce a 0.3 g/mL OGS solution. The OGS solution wasplaced in an incu-shaker at a temperature of 50 °C at 200 rpm for 30 min. The nHA and nMgO (US Research Nanomaterials Inc.) were added into the OGS/ethanol solution. The ceramic/polymer composition for nHA/nMgO/OGS was 29 wt % nHA, 1 wt % nMgO, and 70 wt % OGS. The nHA/nMgO/OGS suspension was sonicated using a high-power sonicator (Qsonica, Q125) for 5 min at 75% of full power (125 W) and mixed using a planetary centrifuge (dual asymmetric centrifugal bladeless high-speed mixer, Speedmixer DAC 150.1 FVZ-K, FlackTek, Inc.) for 5 min at 2500 rpm. The suspension of nHA/nMgO/OGS was mixed for three additional rounds of alternating high-power sonication and high-speed mixing. The nHA and nMgO used in this study were analyzed and published previously.[3,15,34,39,53−55]

The obtained nHA/nMgO/OGS prepolymer mixture was spray coated onto the Mg substrate using the spray coating setup shown in Figure 1. A commercial airbrush (AGPtek 0.3 mm tip 9 cm^3 Dual-Action Gravity Feed Airbrush) with a nozzle diameter of 0.2 mm was set up in a chemical fume hood and supplied with nitrogen gas as a carrier gas. The Mg substrate was held by a 3D printed holder that connected to the electrical spinner. The airbrush was set in a position near the edge of the Mg substrate so that the nHA/nMgO/OGS coating could cover all surfaces (i.e., surface I, surface II, and surface III) of the sample. Specifically, the distance between the edge of the substrate and the nozzle was 6 cm. The angles between the nozzle and *X*-, *Y*-, and *Z*-axes were 70°, 20°, and 90°, respectively. The Mg substrate was spun at 1440 rpm and spray coated at a pressure of 10 psi for 6 s. After spray coating, the metallic substrate was removed from the 3D printed holder, flipped over, and rotated 90° clockwise for an additional round of spray coating, as illustrated by the position change of the red dot on the substrate in Figure 1. After the spray coating process, the entire Mg substrate was fully covered with the polymer-based coating. The nHA/nMgO/OGS coating was cured at 120 °C for 48 h in protective argon gas to obtain nHA/nMgO/PGS nanocomposite coatings. The resulting polymer-based nanocomposite coated Mg samples are referred to as C_A0 (C_Mg), C_A1, C_A3, C_A5, and C_Ti, where "C" represents "nanocomposite coating". The PGS_Mg sample refers to PGS coated Mg, which was fabricated using a method similar to that described above without the addition of the ceramic nanoparticles, and it was used as a control. For the PGS_Mg sample, during the prepolymer preparation, the OGS was mixed with ethanol without the addition of nHA and nMgO.

2.3. Tensile Testing for Interfacial Adhesion Strength of Coatings on Pretreated or Nontreated Mg Substrates. The interfacial adhesion strength of the polymer-based nanocomposites and polymer controls on Mg substrates was tested by following the method described in a previous published work.[3] Specifically, two wooden rods with dimensions of 5 × 5 × 50 mm were attached onto the front and back surfaces of the samples using a cyanoacrylate-based adhesive (Loctite) and allowed to cure for 24 h at room temperature. The wooden rods were then secured in the grip of a tensile tester (Instron 5969). Tensile testing was performed at an extension rate of 1 mm/min. Each group of samples was tested in triplicate.

2.4. Evaluating Nanocomposite Coated Mg Substrates in BMSC Culture In Vitro. Bone marrow derived mesenchymal stem cells (BMSCs) were harvested from femur and tibia of 15 day old Sprague−Dawley rat weanlings after euthanasia according to previously published literature,[5] following the protocol approved by the Institutional Animal and Use Committee (IACUC) at the University of California, Riverside (UCR). BMSCs were cultured in a flask to 90% confluency, collected using Trypsin, and resuspended in fresh medium to achieve a cell seeding density of 10 000 cells/cm^2. The BMSCs were seeded directly onto the surfaces of the samples and cultured with the samples in Dulbecco's Modified Eagle Medium (DMEM, supplemented with 10% FBS and 1% P/S) under standard cell culture conditions (i.e., 37 °C, 95% air, 5% CO_2, sterile, humidified) for 24 h. A0 (Mg), A1, A3, and A5 were used as degradable Mg controls. Ti was used as a nondegradable control, and glass was used as a reference. BMSCs alone in the cell culture medium without samples were used as a positive control, and DMEM alone without BMSCs and samples was used a blank medium reference. All groups were run in triplicate in the culture plate.

After 24 h, the culture medium in each well was collected. The samples and the wells were washed three times with phosphate buffered saline (PBS) to remove nonadherent cells. The cells adhered on the surfaces of the samples (direct contact with the samples) and on the tissue-culture plate surrounding the samples (indirect contact with the samples) were fixed with 4% paraformaldehyde (Electron Microscopy Sciences, 15714-S) and stained with Alexa Fluor 488-phalloidin (Life Technologies) for F-actin and 4′,6-diamidino-2-phenylindole dilactate (DAPI; Life Technologies) for nucleic acid. The cells under direct and indirect contact conditions were imaged using a fluorescence microscope (Nikon Eclipse Ti-S) at 9 random locations using the same exposure conditions and analyzed using

https://doi.org/10.1021/acsami.4c13811
ACS Appl. Mater. Interfaces 2024, 16, 54716−54730

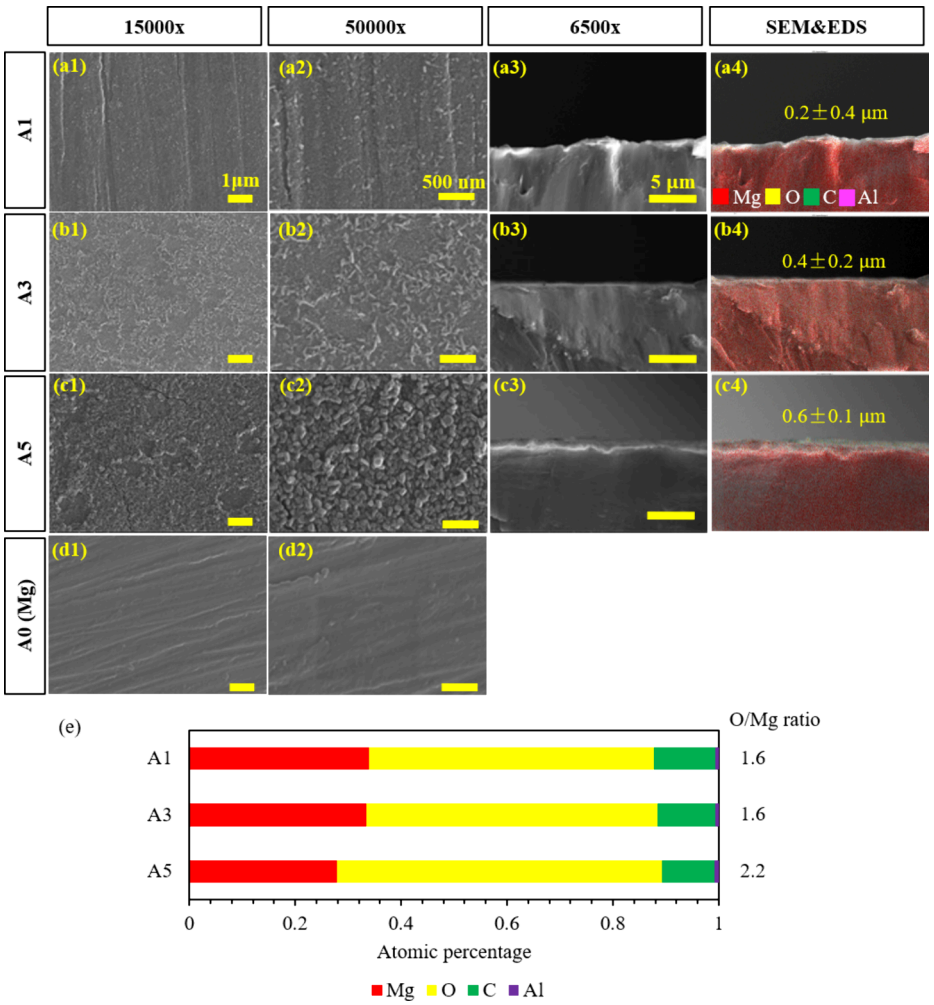

Figure 2. Surface and cross-sectional characterization of alkaline pretreated Mg and nontreated Mg control. SEM images of alkaline pretreated Mg and nontreated Mg control at (a1−d1) a magnification of 15 000× and (a2−d2) a magnification of 50 000×. (a3−c3) Cross-sectional SEM images at a magnification of 6500×. (a4−c4) Overlaid images of SEM and EDS maps for elemental distribution of Mg (red), O (yellow), C (green), and Al (pink). (e) Surface elemental composition (at. %) quantified from EDS area analyses at a magnification of 15 000× and corresponding atomic ratio of O/Mg (at. %/at. %). SEM images for surfaces were obtained at original magnifications of 15 000× and 50 000×; scale bar = 1 μm and 500 nm for original magnifications of 15 000× and 50 000×, respectively. Cross-sectional SEM images and EDS maps were obtained at an original magnification of 6500×; scale bar = 5 μm. The average thickness of the hydroxide layer is marked on the overlaid images of SEM and EDS maps for each sample type, as denoted using the mean ± standard deviation.

ImageJ. The cell adhesion density under direct and indirect contact conditions was calculated as the number of cells per unit area.

The postculture medium was collected after 24 h for pH and ion analyses. The pH of the postculture medium was measured using a precalibrated pH meter (Symphony SB70P, VWR). For ion analysis, the postculture medium was diluted by deionized water with a dilution factor of 100. The concentrations of Mg^{2+} and Ca^{2+} in the diluted postculture medium were analyzed using inductively coupled plasma optical emission spectrometry (ICP-OES; PerkinElmer Optima 8000) to investigate the degradation of Mg substrates and the effects of Mg degradation on Ca^{2+} in the medium with or without cells.

2.5. Characterizing Surface Microstructure, Composition, and Coating Thickness. A scanning electron microscope (SEM; Nova Nano SEM 450, FEI) equipped with an X-Max50 detector and AZtecEnergy software (Oxford Instruments, Abingdon, Oxfordshire, UK) was used to analyze the surface microstructure of the prepared samples. The surfaces of samples were sputter coated (Model 108, Cressington Scientific Instruments Ltd., Watford, UK) with platinum/palladium for 40 s at a current of 20 mA prior to SEM/EDS. Crystalline phases of the alkaline pretreated Mg substrates (i.e., A1, A3, A5) were analyzed using X-ray diffraction (XRD; Empyrean, PANalytical). The thickness of the polymer-based nanocomposites on the Mg substrates was measured using a 3D laser scanning microscope (VK-X150, Keyence). The surface topography of the alkaline pretreated Mg substrates and nontreated Mg control was observed using a 3D laser scanning microscope (VK-X150, Keyence), and the surface roughness (S_q) of the alkaline pretreated Mg was obtained by MultiFileAnalyzer (VK-H1XME, Keyence) according to the established eq 1,[14] where A is the tested area and Z is the deviation in height from the reference plane. The arithmetic mean height (S_a) and maximum height (S_z) were also measured. Equation 2 shows the relationship between S_a and S_q.

$$S_q = \sqrt{\frac{1}{A}\iint_A Z^2(x, y)\,dx\,dy} \quad (1)$$

$$S_a = \frac{S_q}{\sqrt{2}} \quad (2)$$

2.6. Statistical Analysis. All experiments described above were run with triplicate samples. The numerical data were analyzed using standard one-way analysis of variance (ANOVA) when the data sets were parametric (i.e., data normality was over 0.5); statistical

https://doi.org/10.1021/acsami.4c13811
ACS Appl. Mater. Interfaces 2024, 16, 54716−54730

significance was considered at $p < 0.05$ for Tukey's test. When the data sets were nonparametric, the numerical data were examined using the Kruskal–Wallis method followed by a Dunn's test. Statistical significance was considered at $p < 0.025$ for Dunn's test.

3. RESULTS AND DISCUSSION

3.1. Surface, Cross-Sectional Microstructure, and Composition of Mg Substrates before and after Alkaline Pretreatment. Since the hydroxyl groups in the hydroxide layer determine the adhesion strength between the PGS coating and the Mg substrate and affect the corrosion resistance, it is necessary to study the surface characteristics (i.e., surface morphology, elemental composition, surface roughness) of the hydroxide layers formed on Mg substrates after alkaline pretreatments.

Figure 2 shows the surface morphology, elemental composition, and cross-sectional characterization of the alkaline pretreated Mg (i.e., A1, A3, A5) and nontreated Mg control substrates. The SEM images at a magnification of 15 000× (Figure 2a1–d1) show the homogeneous surfaces of the alkaline pretreated Mg and the smoother surface of the nontreated Mg control with observable grinding scratches or polishing grooves. The SEM images at a magnification of 50 000× (Figure 2a2–d2) confirmed the feasibility of the alkaline treatment to produce distinct nanoscale features on the Mg surface. Dense and homogeneous nanoscale features were observed in the SEM images of Mg substrates at high magnification (i.e., 50 000×), without any visible cracks. Moreover, the size of the nanofeatures on the A5 surface was larger than that of the A1 and A3 samples. The increased concentration of the sodium hydroxide (NaOH) solution might have increased the rate of reaction between the Mg surface and NaOH to form $Mg(OH)_2$ and thus accelerated the growth of $Mg(OH)_2$, resulting in a larger size of the nanofeatures on the A5 sample. Furthermore, polishing grooves were still visible on the surface of the A1 sample, which suggested a thinner hydroxide layer on the A1 sample when compared with the A3 and A5 samples. Figure 2a3–c3,a4–c4 represents the cross-sectional SEM images and the corresponding overlaid images of SEM and EDS maps of the Mg and O elemental distribution for the alkaline pretreated Mg substrates. The overlaid images of SEM and EDS maps further confirmed that the oxide layers were created on top of the Mg substrates, with a thickness of 0.2 ± 0.4 μm for A1, 0.4 ± 0.2 μm for A3, and 0.6 ± 0.1 μm for A5. The greater thickness of the oxide layer, the larger size of nanofeatures, and the mismatched thermal expansion coefficient of the $Mg(OH)_2$ with metallic substrates resulted in the visible cracks in the hydroxide layer on A5, as shown in Figure 2c1. Additionally, the thickness of the hydroxide layer on the A1 sample was thinner on average than that on the A3 and A5 samples, in agreement with the visible polishing grooves in the SEM images of the A1 sample.

The histogram in Figure 2e shows the surface elemental compositions (in at. %) of the alkaline pretreated Mg quantified from the EDS analyses based on the SEM images at a magnification of 15 000×. Mg and oxygen (O) were detected on A1, A3, and A5 samples. A small amount of carbon (C) could have come from the conductive carbon tape under the Mg substrates, and aluminum (Al) was the alloying element in the Mg substrate. The atomic ratio of O/Mg for the A5 sample was 2.2, which was closest to the stoichiometric ratio of $Mg(OH)_2$. The atomic ratios of O/Mg for the A1 and A3 samples were both 1.6, possibly because the pretreated Mg surface layers consisted of an inner MgO layer next to the substrate and an external layer of $Mg(OH)_2$.[45] Table 1 shows the surface roughness of Mg samples before and after the alkaline treatment. The surface roughness of the alkaline pretreated Mg samples (i.e., A1, A3, A5) was larger than that of the nontreated Mg control.

Table 1. Surface Roughness of Mg Substrates before and after Alkaline Treatment in NaOH at Concentrations of 1, 3, and 5 M

sample ID	roughness (μm)	before alkaline treatment	after alkaline treatment
A1	S_q	0.105 ± 0.007	0.143 ± 0.011
	S_a	0.072 ± 0.005	0.107 ± 0.008
	S_z	1.680 ± 0.014	1.885 ± 0.05
A3	S_q	0.088 ± 0.007	0.151 ± 0.012
	S_a	0.070 ± 0.005	0.115 ± 0.004
	S_z	2.465 ± 0.043	2.505 ± 0.024
A5	S_q	0.059 ± 0.008	0.082 ± 0.011
	S_a	0.046 ± 0.036	0.057 ± 0.005
	S_z	1.385 ± 0.043	3.815 ± 0.153

The XRD patterns in Figure 3 show low-intensity diffraction peaks for the crystalline phase of $Mg(OH)_2$ (ICSD pattern 00-050-1085), which is consistent with previous studies that also showed low-intensity peaks of $Mg(OH)_2$ on the Mg alloy after pretreatment with NaOH solution.[45,47,49,50] The α-Mg phase (ICDD 00-004-0770) and intermetallic $Al_{0.05}Mg_{1.95}$ (ICDD 00-041-1238) from the underlying Mg substrate showed higher-intensity peaks. In contrast, the intensity of the $Mg(OH)_2$ peak was lower probably because of its thin thickness and dominating peaks from the Mg substrate.

3.2. Surface, Cross-Sectional Microstructure, and Composition of Polymer-Based Nanocomposites on Mg Substrates. The spray coating process generated homogeneous polymer nanocomposite layers on the Mg substrates. The results of surface and cross-sectional characterizations in Figures 4–6 do not show visible pores and cracks after spray coating.

Figure 4a shows the surface morphology of the polymer-based nanocomposites on Mg substrates (i.e., C_A1, C_A3, C_A5, C_Mg), characterized using SEM at an original magnification of 10 000×, and the overlaid images of SEM and EDS elemental maps, as well as the corresponding EDS maps for the individual elements C, O, calcium (Ca), phosphorus (P), and Mg. Each color represents a single element, where green = C, yellow = O, purple = Ca, pink = P, and red = Mg. The location of agglomerates in the SEM images overlapped with the regions of intensified Ca, P, and O elements in the EDS maps, indicating that the agglomerates on the coated C_A1, C_A3, C_A5, and C_Mg samples contained hydroxyapatite (HA). Furthermore, elemental Mg was distributed homogeneously in its EDS map, suggesting that the MgO nanoparticles were distributed homogeneously in the nanocomposite coatings for all samples. Elemental C was distributed evenly in its EDS maps as well, except a reduced signal was observed around the agglomerates, indicating that the C signal came from the PGS polymer matrix.

The histogram in Figure 4b shows the surface elemental compositions (in at. %) of the polymer-based nanocomposites on the Mg substrates, which were quantified from EDS

https://doi.org/10.1021/acsami.4c13811
ACS Appl. Mater. Interfaces 2024, 16, 54716–54730

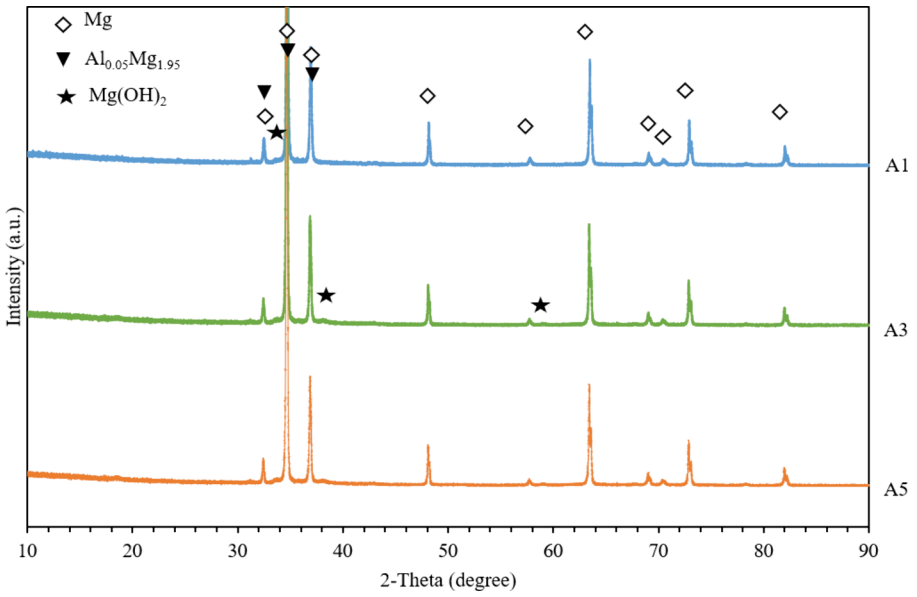

Figure 3. X-ray diffraction patterns of alkaline pretreated Mg.

analyses on the same SEM images taken at a magnification of 10 000×. It shows that the nanocomposite coatings for C_A1, C_A3, C_A5, and C_Mg were mainly composed of C and O with a small amount of Ca and P elements from the HA nanoparticles and Mg element from the MgO nanoparticles, which further confirmed that the polymer-based nanocomposite coatings covered the entire surface of the Mg substrates.

Figure 5 shows the cross-sectional SEM images of the C_A1 sample and C_Mg control at magnifications of 1000× and 10 000× and the overlaid images of SEM and EDS maps, as well as the corresponding EDS maps for the individual elements C, O, Ca, P, and Mg. Each color represents a single element, where green = C, yellow = O, purple = Ca, orange = P, and red = Mg. The overlaid images of SEM and EDS at the same magnification of 1000× were used to determine the interface between the coatings and substrates. The thickness of the polymer-based nanocomposite coatings on the Mg substrate was 57.0 ± 3.0 μm for the C_A1 sample and 27.6 ± 2.4 μm for the C_Mg sample. The overlaid cross-sectional SEM and EDS images at a magnification of 10 000× indicated that the HA and MgO nanoparticles were uniformly dispersed in the polymer matrix. Moreover, no visible holes and cracks were observed in the cross-sectional view, indicating that the nanoparticles were integrated into the polymer matrix. The cracks along the interface between the polymer-based nanocomposite coating and the Mg substrate were possibly caused by sample preparation (cross-sectional cutting) prior to SEM. The cross-sectional EDS maps for the elemental distribution of C, O, Ca, P and Mg show that the polymer-based nanocomposite coatings were mainly composed of C and O elements, with the Ca, P, and Mg elements uniformly distributed throughout the polymer matrix, which further confirmed that the nanoparticles were evenly dispersed in the polymer matrix.

The thickness of the polymer-based nanocomposites on Mg substrates was also analyzed by using a 3D laser scanning microscope. Figure 6 shows the surface morphology and thickness of the polymer-based nanocomposites on Mg substrates (i.e., C_A1, C_A3, C_A5, and C_Mg). The laser and optical images in Figure 6a show that the polymer-based nanocomposite coatings were homogeneous. Figure 6b–d shows the thickness measurements of surface I, surface II, and surface III, obtained by a 3D laser scanning microscope. The green lines and yellow lines in the images represent the linear profiles of the polymer-based nanocomposite coatings and the underlaying Mg substrates, respectively. The relatively flat green linear profiles of surface I and surface II (Figure 6b,c) for all the samples demonstrated that the polymer-based nanocomposites were smooth, homogeneous, and evenly distributed on the Mg substrates. The yellow linear profiles for the pretreated and nontreated Mg substrates had noise of peaks and valleys, which could be caused by the rough surface of the hydroxide layers and/or the polishing grooves. The green and yellow linear profiles of surface III for all samples showed large fluctuations with an arc shape in thickness when compared with those of surface I and surface II, which could be caused by the relative position of the spray nozzle toward different surfaces and significant surface tension during spray coating.

The average thicknesses of surface I for C_A1, C_A3, C_A5, and C_Mg samples were 42.3 ± 1.4, 42.6 ± 4.7, 44.3 ± 3.0, and 43.8 ± 4.2 μm, respectively. The average thicknesses of surface II for C_A1, C_A3, C_A5, and C_Mg samples were 37.7 ± 3.3, 36.9 ± 3.2, 34.5 ± 2.1, and 40.9 ± 3.9 μm, respectively. The average thicknesses of surface III for C_A1, C_A3, C_A5, and C_Mg samples were 32.7 ± 23.7, 29.3 ± 10.2, 27.5 ± 13.2, and 36.6 ± 10.8 μm, respectively. The thickness measurements also show that the thicknesses of surfaces I and II were relatively uniform with small standard deviations, while the thickness of surface III had large standard deviations.

3.3. Interfacial Adhesion Strength of Polymer Nanocomposite Coatings on Pretreated or Nontreated Mg Substrates. Figure 7a,b shows the schematic illustration and actual photograph of the experimental setup for measuring the interfacial adhesion strength. Figure 7b shows that the polymer-based nanocomposite coating on Mg was partially peeled off after the tensile test. Figure 7c shows the interfacial adhesion strength of polymer-based nanocomposites on Mg substrates (i.e., C_A1, C_A3, C_A5, C_Mg) and that of the

https://doi.org/10.1021/acsami.4c13811
ACS Appl. Mater. Interfaces 2024, 16, 54716−54730

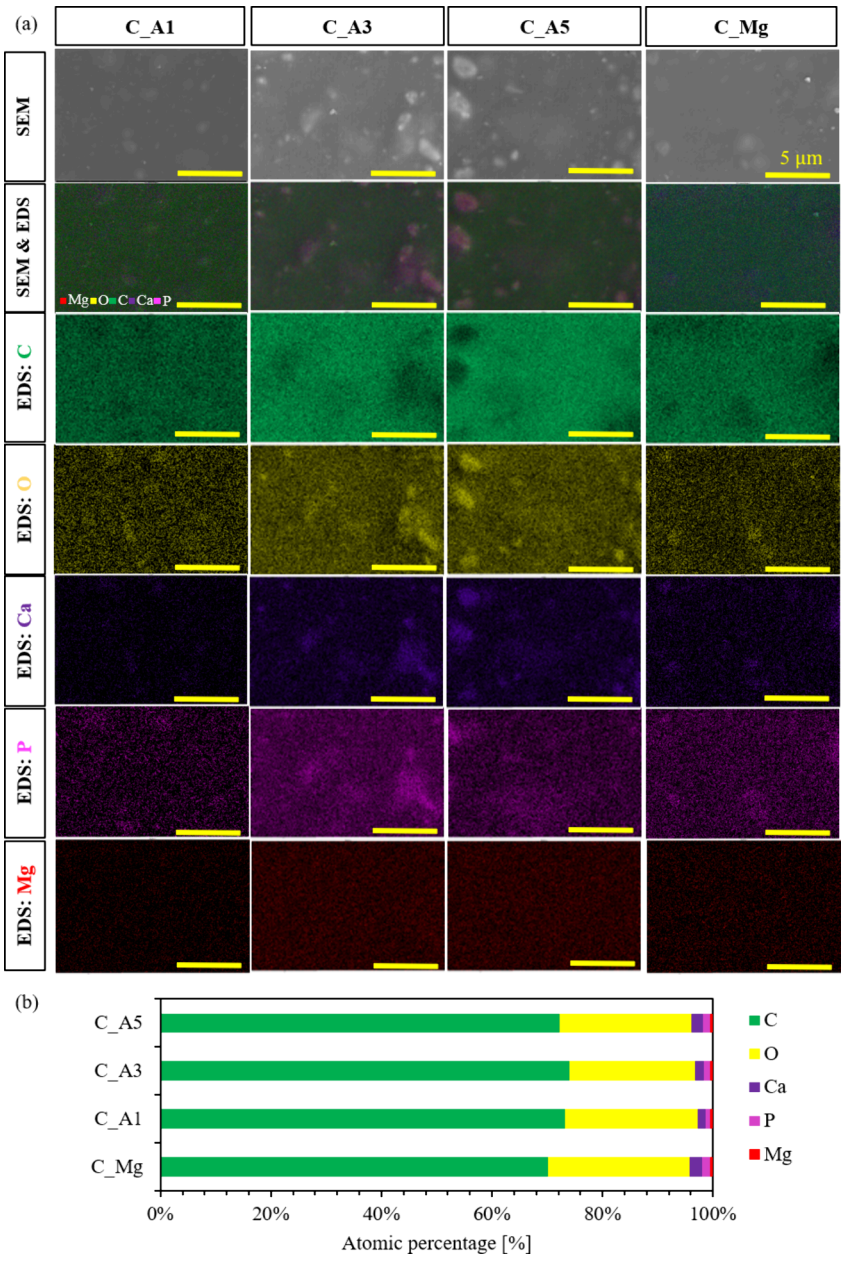

Figure 4. Surface characterization of polymer nanocomposite coatings on the pretreated and nontreated Mg. (a) SEM images and corresponding overlaid SEM images and EDS maps of C (green), O (yellow), Ca (purple), Mg (red), and P (pink), as well as the individual EDS maps of different elements: C (green), O (yellow), Ca (purple), P (pink), and Mg (red). (b) Surface elemental composition (at. %) quantified from EDS area analyses at a magnification of 10 000×. SEM images and EDS maps were obtained at an original magnification of 10 000×; scale bar = 5 μm.

polymer control without nHA and nMgO on the Mg substrate (PGS_Mg). The statistical analysis on the interfacial adhesion strength was tested using one-way ANOVA because the data sets were parametric. When compared with the PGS_Mg sample, the interfacial adhesion strength of the C_A1, C_A3, C_A5, and C_Mg samples was significantly enhanced, indicating the nanophase HA and MgO dispersed in the PGS matrix could improve the adhesion strength of PGS coatings on Mg substrates. Moreover, the C_A1 and C_A3 samples demonstrated stronger adhesion strength on average than the C_Mg sample, suggesting that the alkaline pretreatment of Mg substrates could improve the interfacial adhesion strength of the polymer-based nanocomposite coatings.

PGS is a semicrystalline polymer.[56] In the nHA/nMgO/PGS nanocomposite system, the nHA and nMgO serve as the nucleating agents for PGS,[57−59] which could consequently increase the crystallization and reduce the grain size. During the curing process, the polymer-based coating usually undergoes shrinkage, which would induce internal stress.[3] The internal stress could cause crack propagation in the coating and therefore reduce its adhesion strength. When compared with PGS_Mg, the smaller crystals in C_A1, C_A3, C_A5, and C_Mg samples could restrict the crack propagation more effectively than the larger crystals in PGS_Mg,[60] which could enhance the interfacial adhesion strength. Furthermore, the presence of dispersed nanoparticles and increased nucleation of PGS crystals on the Mg substrates could provide more sites (areas) for interfacial interactions, which could also enhance the interfacial adhesion strength.[61] In addition, the nHA and nMgO have high strength and moduli,[55] and they could absorb

https://doi.org/10.1021/acsami.4c13811
ACS Appl. Mater. Interfaces 2024, 16, 54716−54730

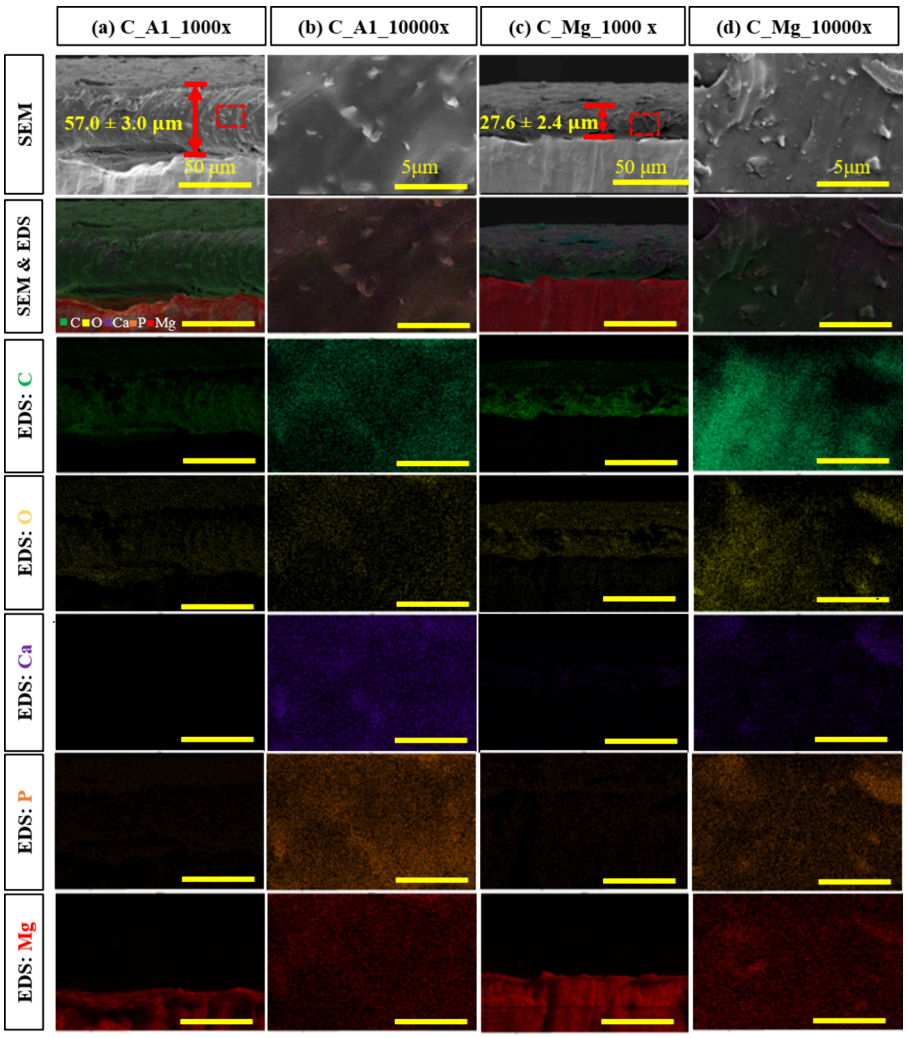

Figure 5. Analyses of cross sections of polymer nanocomposite coatings on the pretreated and nontreated Mg. (a) C_A1 at an original magnification of 1000×, (b) C_A1 at an original magnification of 10 000×, (c) C_Mg at an original magnification of 1000×, (d) C_Mg at an original magnification of 10 000×, and corresponding overlaid SEM images and EDS maps of C (green), O (yellow), Ca (purple), P (orange), and Mg (red), as well as individual EDS maps of different elements: C (green), O (yellow), Ca (purple), P (orange), and Mg (red).

large amounts of internal stress and improve the interfacial adhesion strength as a reinforcement phase in the polymer-based nanocomposites.

The alkaline pretreatment has a significant influence on improving the interfacial adhesion strength of polymer-based nanocomposites on the Mg substrates. The average interfacial adhesion strength of C_A1 is 6.6 MPa, which is 8.2% higher than that of C_Mg. The C_A3 sample showed the highest average interfacial adhesion strength (7.4 MPa) among all samples, which is 22% higher than that of C_Mg. The improvement in the interfacial adhesion strength of C_A3 and C_A1 could be ascribed to the hydroxyl groups in the $Mg(OH)_2$ layer formed on the surface of the Mg substrate after alkaline treatment, facilitating the formation of strong chemical bonds at the interface. When compared with C_Mg, the average interfacial adhesion strength of C_A5 was slightly reduced, which was possibly because of the visible cracks in the $Mg(OH)_2$ layer of the A5 sample, as shown in Figure 2c1. The visible cracks in the A5 sample acted as discontinuities in the coating, where internal stress increased sharply,[62] and reduced the interfacial adhesion strength.

The adhesion strength of $Mg(OH)_2$ on Mg substrates is expected to be significantly higher due to the presence of chemical bonding formed at the interface during the chemical reaction. The thickness and structure of the $Mg(OH)_2$ layer could be further optimized. From our study, the thicker the formed nanostructured $Mg(OH)_2$ layers on the surface of the Mg substrate were, the more visible mini-cracks started to appear on the samples. The overall composite coating stability is considered to be the main factor that affects the overall adhesion strength and causes coating failure since the adhesion strength of $Mg(OH)_2$ is expected to be higher due to the presence of chemical bonding formed at the interface. More studies are needed in the future to further optimize the interfacial strength of the polymer nanocomposite coatings to the $Mg(OH)_2$ layer and the $Mg(OH)_2$ layer to the Mg substrate.

3.4. Composition of the Medium after 24 h Cell Culture. The postculture media cultured with the samples were analyzed to study the in vitro degradation of the materials of interest, as shown in Figure 8. Figure 8a shows the pH of the collected media after 24 h of BMSC culture with the samples. The statistical analysis for pH was tested using one-way

https://doi.org/10.1021/acsami.4c13811
ACS Appl. Mater. Interfaces 2024, 16, 54716−54730

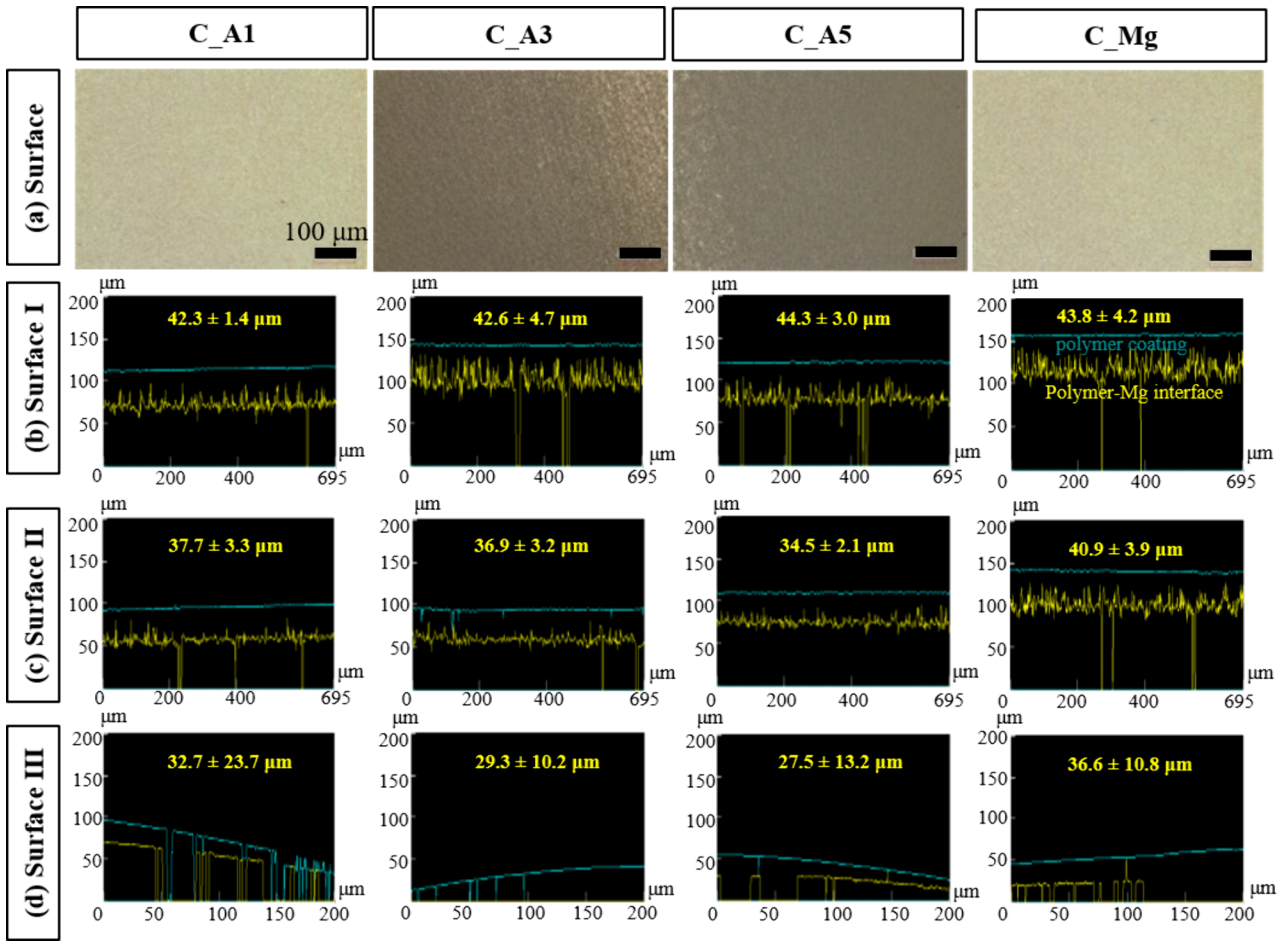

Figure 6. Surface morphology and thickness of the polymer-based nanocomposites on Mg substrates. (a) Optical and laser images for C_A1, C_A3, C_A5, and C_Mg. (b–d) Surface linear profiles of the polymer-based nanocomposites on Mg substrates obtained using a 3D laser scanning microscope: (b) surface linear profile for front surface (surface I), (c) surface linear profile for back surface (surface II), and (d) surface linear profile for the side surface (surface III). The green lines represent the linear profiles of the polymer-based nanocomposite coatings, and the yellow lines represent the interface between the coating and the Mg substrate. The average thickness of the polymer-based nanocomposite coatings is marked on the surface linear profiles, denoted using the mean ± standard deviation. The optical and laser images were taken at an original magnification of 480×; scale bar = 100 μm.

ANOVA because the data sets were parametric. ANOVA confirmed that the pH in the medium cultured with PGS_Mg was significantly higher than that of the glass reference and Ti and BMSC controls. The pH in the medium cultured with the C_Ti sample was significantly lower than that of the PGS_Mg, A1, A3, A5, and Mg control samples. No significant differences in pH were found among other groups. The pH change of the postculture medium was associated with the degradation of the samples. The C_A1, C_A3, C_A5, C_Mg, A1, A3, and A5 samples had a higher average pH when compared with the nondegradable Ti control, glass reference, BMSC alone, and medium alone, suggesting degradation of the Mg substrate, the dissociation of the $Mg(OH)_2$ layer, or the dissociation of the nMgO in the polymer coatings. Moreover, the PGS/nHA/nMgO coated Ti (C_Ti) had a lower average pH when compared with the nondegradable Ti control, glass reference, BMSC alone, and medium alone, indicating the polymer-based nanocomposites on Mg substrates could lower the pH of the medium because of PGS degradation. Liang et al.[63] reported a similar change of pH for PGS scaffold in the culture medium of DMEM (i.e., pH was 0.4 lower than the blank medium), which was ascribed to the ionization of the unreacted carboxylic acid (−COOH) groups in PGS or the carboxylic acid groups formed by hydrolysis of the PGS ester (−COOR) groups. In our case of polymer-based nanocomposite coated Ti, the MgO particles could dissociate with water, resulting in the release of Mg ions and hydroxide ions to form metallic carboxylates and water molecules, which could neutralize the acidity in the medium (i.e., pH was only 0.08 lower than the blank medium in this study). The polymer-based nanocomposites on Mg substrates had lower average pH values when compared with the polymer control on the Mg substrate, indicating slower Mg degradation of the nanocomposite coated Mg. The faster degradation of the polymer control on Mg (PGS_Mg) is possibly because of its poor interfacial adhesion strength when compared with that of the nanocomposites on Mg.

Figure 8b shows the Mg^{2+} ion concentration in the collected media after 24 h of BMSC culture with the samples. One-way ANOVA was used to determine the statistically significant differences in the $[Mg^{2+}]$ of the collected media for all groups of samples because the data sets were parametric. The Mg^{2+} ions in the culture media could come from the degradation of the Mg substrates, the dissociation of the interfacial $Mg(OH)_2$ layers, or the nMgO particles in the polymer matrix. It was found that the C_Mg (C_A0) and C_A1 samples had significantly higher $[Mg^{2+}]$ than the C_Ti, A1, A3, A5, Mg, Ti

https://doi.org/10.1021/acsami.4c13811
ACS Appl. Mater. Interfaces 2024, 16, 54716−54730

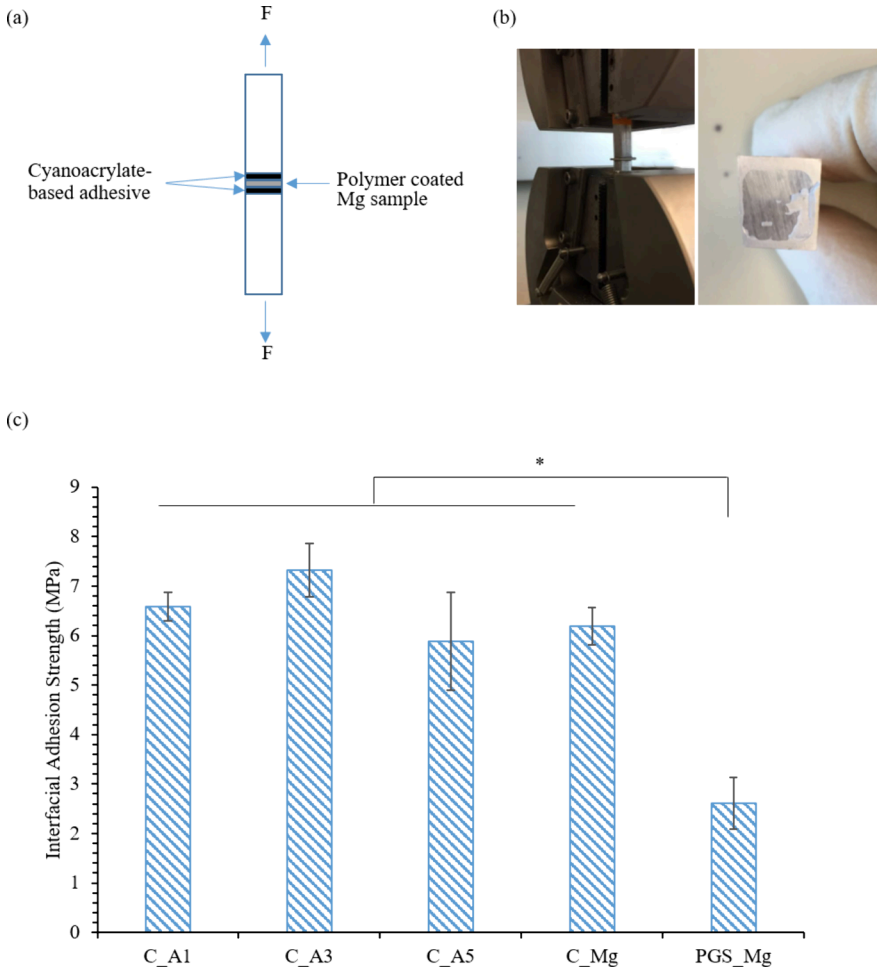

Figure 7. Analysis of the interfacial adhesion strength of the polymer-based nanocomposites and polymer control on Mg substrates. (a) Schematic illustration of the experimental setup for measuring the interfacial adhesion strength. (b) Photograph showing the actual experimental setup for measuring the interfacial adhesion strength and an image of the polymer-based nanocomposite on Mg after the tensile test. Tensile testing was performed to measure the maximum force needed to delaminate the coating from the substrate. (c) Adhesion strength between the coating and the substrate for C_A1, C_A3, C_A5, C_Mg, and PGS_Mg control, calculated from the maximum force. Values are mean ± standard deviation; $n = 3$. *$p < 0.05$.

control, glass reference, BMSC alone (without samples), and medium alone (without BMSCs and samples). The C_A3 sample had a significantly higher $[Mg^{2+}]$ than the C_Ti, A1, A5, Mg, Ti control, glass reference, BMSC alone, and medium alone. The C_A5 sample had a significantly higher $[Mg^{2+}]$ than the C_Ti, A5, Ti control, glass reference, BMSC alone, and medium alone. The $[Mg^{2+}]$ in the media cultured with the polymer-based nanocomposites on Mg (i.e., C_A0, C_A1, C_A3, and C_A5) was significantly higher when compared with that for the corresponding nontreated and treated Mg substrates (i.e., A0, A1, A3, and A5). For the polymer-based nanocomposites on Mg, the Mg^{2+} ions in the culture media could come from the degradation of Mg substrates or the dissociation of the interfacial $Mg(OH)_2$ layers, and it could also come from the dissociation of the nMgO particles in the polymer-based nanocomposites during incubation, which could lead to a higher amount of $[Mg^{2+}]$ in the culture medium when compared with the Mg substrates. The $[Mg^{2+}]$ in the medium cultured with the PGS_Mg (PGS_A0) sample was significantly higher than that for the C_Ti, A1, A5, Mg, Ti control, glass reference, BMSC alone, and medium alone. The $[Mg^{2+}]$ in the medium cultured with the PGS_Mg had a good correlation with the change of pH, shown in Figure 8a; both were higher on average as compared with the other groups, possibly because the weak interfacial adhesion strength between the PGS coating and the underlying Mg substrate could cause faster Mg degradation for the PGS_Mg sample. The A1 sample had a significantly higher $[Mg^{2+}]$ when compared with the C_Ti sample, possibly because the A1 treated Mg released more Mg^{2+} ions than the nanocomposite in the 24 h culture. Moreover, the $[Mg^{2+}]$ in the media cultured with the respective A1, A3, and A5 samples and the Mg control were significantly higher than that for the Ti control, glass reference, BMSC alone, and medium alone.

Figure 8c shows the Ca^{2+} concentration in the collected media after 24 h of BMSC culture with the samples. The Kruskal–Wallis method was used to determine the statistically significant differences in the $[Ca^{2+}]$ of the collected media for all groups of samples because the data sets were non-parametric. No statistically significant differences in the $[Ca^{2+}]$ of the collected media were found among all groups of samples.

3.5. BMSC Adhesion and Morphology after 24 h Culture with the Samples. The fluorescence images of BMSC adhesion and morphology under direct and indirect contact with the experimental groups and controls in 24 h of

https://doi.org/10.1021/acsami.4c13811
ACS Appl. Mater. Interfaces 2024, 16, 54716−54730

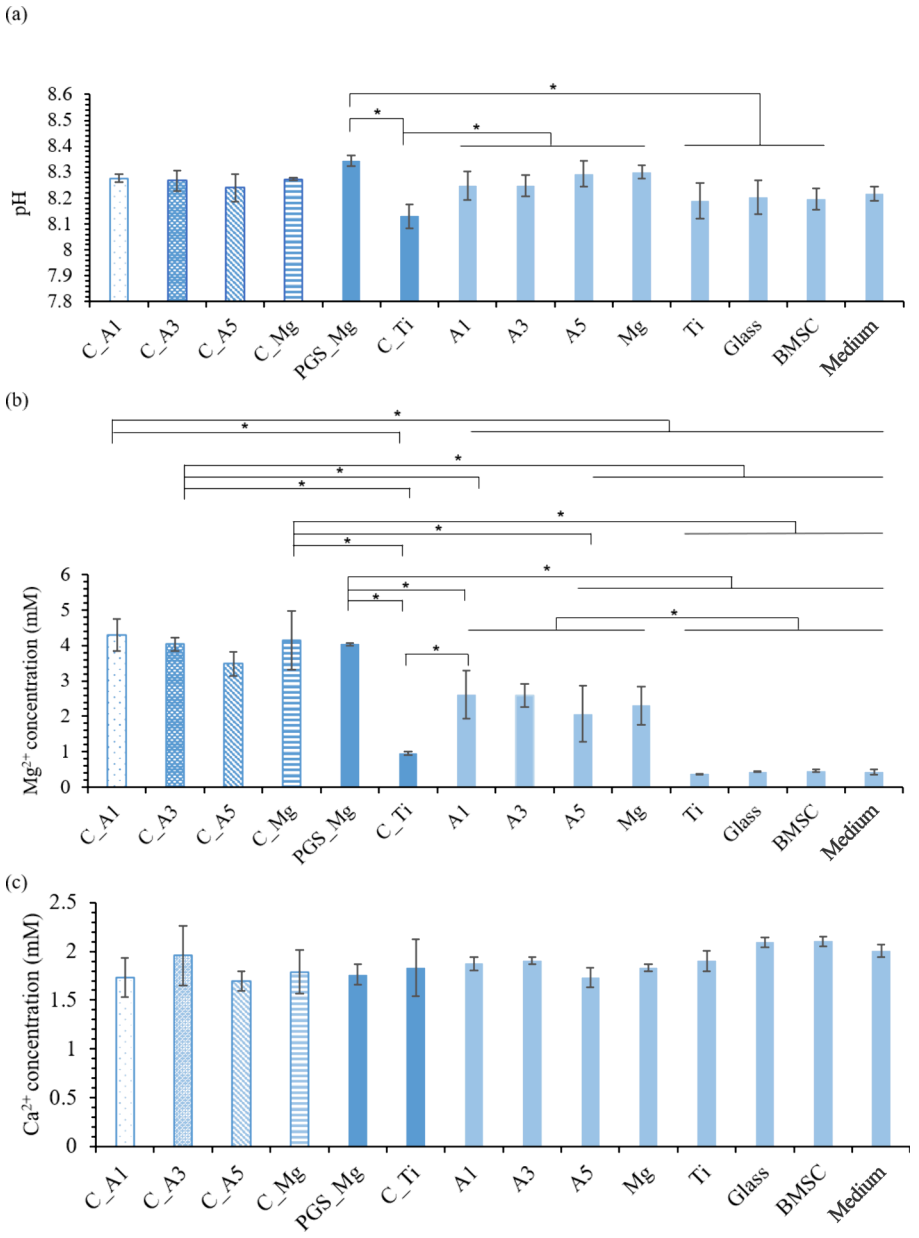

Figure 8. Postculture analysis of media after direct culture of BMSCs with the materials of interest in DMEM for 24 h. (a) pH, (b) Mg^{2+} concentration, and (c) Ca^{2+} concentration of the collected BMSC culture media. Values are mean ± standard deviation; $n = 3$. $^{*}p < 0.05$.

direct culture are summarized in Figure 9. All the samples and controls showed the attachments of viable BMSCs, but the cells on the glass reference, Ti, and BMSC controls under direct contact had a higher spreading area when compared with the polymer-based nanocomposites on Mg (i.e., C_A1, CA3, C_A5, and C_Mg), C_Ti, PGS_Mg, alkaline pretreated Mg (i.e., A1, A3, A5), and nontreated Mg control. Under indirect contact conditions, the cells attached on the plates around the samples showed a similar spreading area to the controls and reference, except the cells adhered on the well plate around the C_Ti showed reduced spreading. BMSC adhesion densities under direct and indirect contact with the samples, as well as the controls and reference, are summarized in Figure 10. The adhesion density was analyzed using one-way ANOVA because the data sets were parametric. There were no statistically significant differences in BMSC adhesion density under direct contact with the samples. Under indirect contact, ANOVA confirmed a significantly lower BMSC adhesion density around C_Ti than the glass reference and BMSC positive control, likely because of PGS; additionally, the A3, A5, and nontreated Mg (A0) control also had significantly lower BMSC adhesion densities when compared with the glass reference. No significant differences in BMSC adhesion density was found among the other groups under indirect contact.

Though no significant differences in the BMSC adhesion density under direct contact were found among all groups of samples, the polymer-based nanocomposites on Mg substrates (i.e., C_A1, CA3, C_A5, and C_Mg) showed higher average BMSC adhesion densities than the PGS_Mg, pretreated Mg (i.e., A1, A3, A5), and nontreated Mg control, indicating that the nHA and nMgO in the polymer-based nanocomposites were beneficial for BMSC adhesion. Moreover, the polymer-based nanocomposites on Mg (i.e., C_A1, CA3, C_A5, and C_Mg) had higher average BMSC adhesion densities than

https://doi.org/10.1021/acsami.4c13811
ACS Appl. Mater. Interfaces 2024, 16, 54716−54730

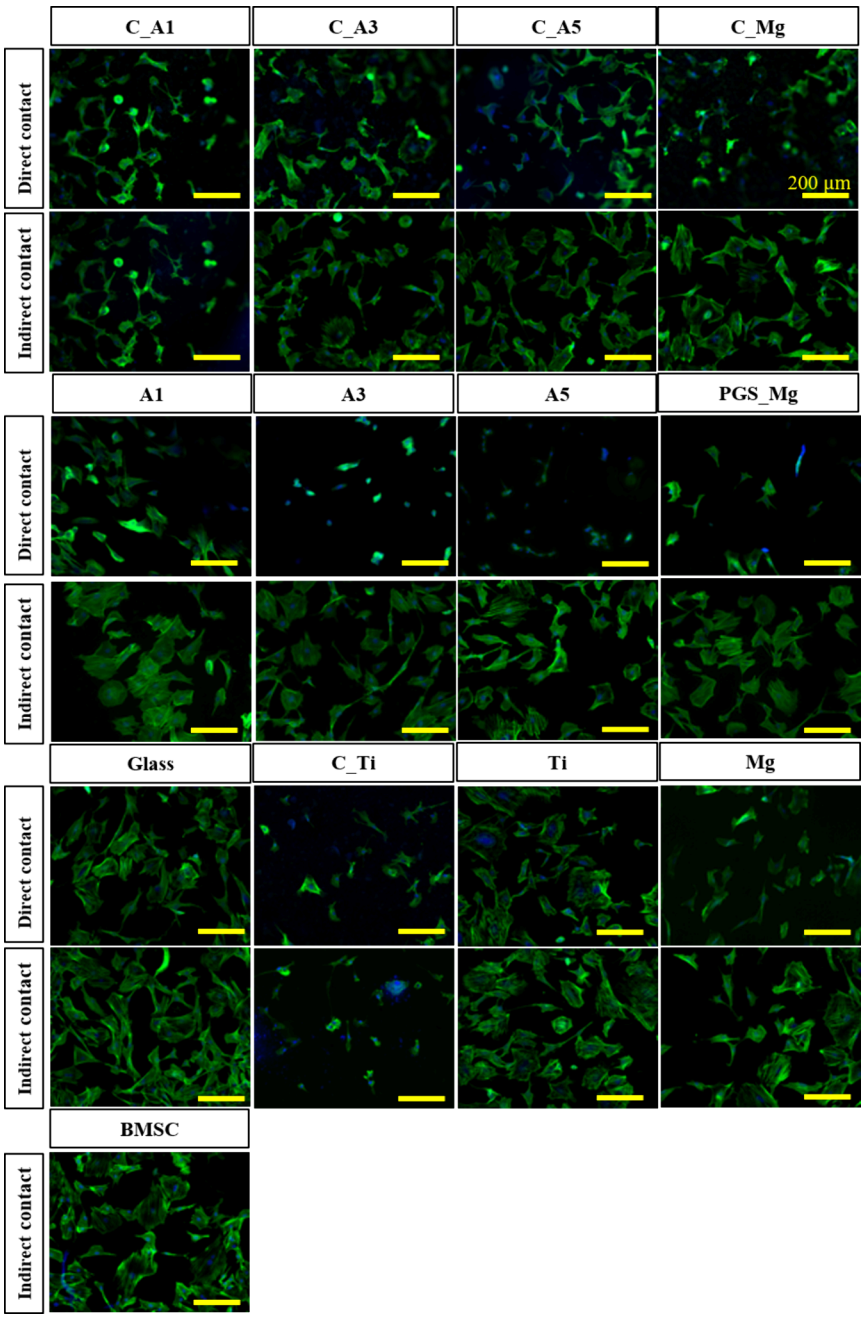

Figure 9. Fluorescence images of BMSCs after direct culture with the materials of interest in DMEM for 24 h. Fluorescence images of BMSCs adhered on the sample surfaces (labeled as "direct contact") and on the culture plates surrounding the samples (labeled as "indirect contact"). Blue color indicates DAPI stained nuclei, and green color indicates Alexa Fluor 488-phalloidin stained F-actin (cytoskeleton). Scale bar = 200 μm for all images. Original magnification = 10×.

C_Ti, indicating that the Mg^{2+} released from the underlying Mg substrate could promote BMSC adhesion. Therefore, the increased BMSC adhesion on the polymer-based nanocomposite coated Mg substrates (i.e., C_A1, CA3, C_A5, and C_Mg) could be ascribed to the synergic effects of the nHA, nMgO, and increased Mg^{2+} concentrations. Johnson et al. reported an increased BMSC adhesion density on nHA/PCL nanocomposite coated Mg when compared with an nHA/PCL nanocomposite film and nontreated Mg control, which agrees with our findings mentioned above. It has been known that MgO exhibits a stimulating effect on bone healing and regeneration in rat tibia as an implantable paste,[36] and HA is a component naturally found in human bone that can enhance bone regeneration because of its osteoconductive and osteoinductive properties.[64,65]

4. CONCLUSION

This study reported a spray coating process for coating polymer-based nanocomposites and a polymer control on all six surfaces of Mg substrates to ensure the homogeneity of the surface morphology and composition. The surface microstructure, elemental composition, and thickness of the Mg substrates before and after alkaline treatment were studied. The higher the alkaline solution concentration (i.e., 1, 3, 5 M), the thicker the formed nanostructured $Mg(OH)_2$ layers on the surface of the Mg substrate, and visible mini-cracks were found

https://doi.org/10.1021/acsami.4c13811
ACS Appl. Mater. Interfaces 2024, 16, 54716−54730

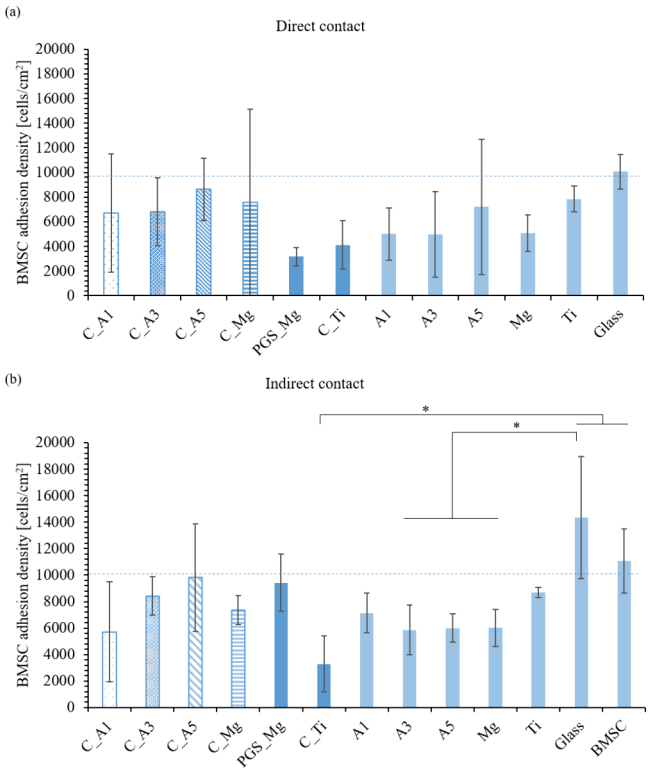

Figure 10. Adhesion densities of BMSCs after direct culture with the materials of interest in DMEM for 24 h. (a) BMSC adhesion density on the sample surfaces (labeled as "direct contact") and (b) BMSC adhesion density on the culture plates surrounding the samples (labeled as "indirect contact"). Values are mean ± standard deviation; $n = 3$. *$p < 0.05$.

on the samples that were alkaline treated in 5 M NaOH solution. The $Mg(OH)_2$ layers on Mg and the addition of nHA and nMgO particles to the PGS both contributed to the improvement of the interfacial adhesion strength between the polymer-based nanocomposites and the underlying Mg substrates, in which C_A3 showed the highest average adhesion strength among all groups. Moreover, the polymer-based nanocomposites on Mg substrates (i.e., C_A1, C_A3, C_A5, and C_Mg) had higher average BMSC adhesion densities under direct and indirect contact when compared with their corresponding Mg controls (i.e., A1, A3, A5, and Mg). The addition of nHA and nMgO in the polymer-based nanocomposites on Mg substrates also increased the BMSC adhesion density under direct contact when compared with the polymer control on Mg substrate (i.e., PGS_Mg). Apart from the addition of nHA and nMgO to the PGS coating, the release of Mg^{2+} from the underlying Mg substrates could offer a synergetic effect of enhancing BMSC adhesion under direct and indirect contact when compared with the polymer-based nanocomposite on Ti (i.e., C_Ti). In summary, the C_A3 sample in this study provided the optimal results in increasing the interfacial adhesion strength and improving the BMSC adhesion density.

This study presented homogeneous polymer nanocomposite coatings on Mg substrates via a spray coating process in combination with pretreatment of the Mg substrates. The overall process enhanced the interfacial adhesion strength of the coatings and improved degradation properties and BMSC adhesion, which are valuable for skeletal implant applications and bone tissue engineering applications. The biodegradable nanocomposites and the coating processes on biodegradable Mg substrates developed in this study are transferable for many different biomedical applications such as biodegradable internal fixation devices for bone repair, drug-eluting coatings and devices, and biodegradable and biocompatible tissue scaffolds for regenerative medicine.

AUTHOR INFORMATION

Corresponding Author

Huinan Hannah Liu − *Department of Bioengineering, Materials Science & Engineering Program, and Stem Cell Center, University of California, Riverside, Riverside, California 92521, United States;* orcid.org/0000-0001-9366-6204; Phone: 951 827 2944; Email: huinan.liu@ucr.edu; Fax: 951 827 6416

Authors

Xijuan Chai − *Department of Bioengineering, University of California, Riverside, Riverside, California 92521, United States; Department of Material Science and Technology, Southwest Forestry University, Kunming 650224, P.R. China*

Jiajia Lin − *Materials Science & Engineering Program, University of California, Riverside, Riverside, California 92521, United States*

Changlu Xu − *Materials Science & Engineering Program, University of California, Riverside, Riverside, California 92521, United States;* orcid.org/0000-0001-5968-2462

Dongwei Sun − *Department of Bioengineering and Materials Science & Engineering Program, University of California, Riverside, Riverside, California 92521, United States*

Complete contact information is available at: https://pubs.acs.org/10.1021/acsami.4c13811

Author Contributions

#X.C. and J.L. are co-first authors who contributed equally.

Notes

Any opinions, findings, and conclusions or recommendations expressed in this material are those of the authors and do not necessarily reflect the views of the funding agencies.
The authors declare no competing financial interest.

ACKNOWLEDGMENTS

The authors would like to thank the University of California, Riverside for the Dissertation Research Grant (J.L.) and Dissertation Year Program Award (J.L. and C.X.). The authors would like to thank the Central Facility for Advanced Microscopy and Microanalysis (CFAMM) at the University of California, Riverside for the use of the SEM/EDS and Dr. Perry Cheung for the XRD instrument training.

REFERENCES

(1) Johnson, I.; Perchy, D.; Liu, H. In vitro evaluation of the surface effects on magnesium-yttrium alloy degradation and mesenchymal stem cell adhesion. *J. Biomed. Mater. Res., Part A* **2012**, *100* (2), 477−485.

(2) Iskandar, M. E.; Aslani, A.; Tian, Q.; Liu, H. Nanostructured calcium phosphate coatings on magnesium alloys: characterization and cytocompatibility with mesenchymal stem cells. *J. Mater. Sci.: Mater. Med.* **2015**, *26* (5), 189.

(3) Johnson, I.; Wang, S. M.; Silken, C.; Liu, H. A systemic study on key parameters affecting nanocomposite coatings on magnesium substrates. *Acta biomaterialia* **2016**, *36*, 332−349.

(4) Lock, J. Y.; Wyatt, E.; Upadhyayula, S.; Whall, A.; Nunez, V.; Vullev, V. I.; Liu, H. Degradation and antibacterial properties of magnesium alloys in artificial urine for potential resorbable ureteral stent applications. *J. Biomed. Mater. Res., Part A* **2014**, *102* (3), 781−792.
(5) Cipriano, A. F.; Lin, J.; Miller, C.; Lin, A.; Alcaraz, M. C. C.; Soria, P., Jr; Liu, H. Anodization of magnesium for biomedical applications-Processing, characterization, degradation and cytocompatibility. *Acta Biomater.* **2017**, *62*, 397−417.
(6) Witte, F.; Hort, N.; Vogt, C.; Cohen, S.; Kainer, K. U.; Willumeit, R.; Feyerabend, F. Degradable biomaterials based on magnesium corrosion. *Curr. Opin. Solid State Mater. Sci.* **2008**, *12* (5−6), 63−72.
(7) Gu, X.-N.; Zheng, Y.-F. A review on magnesium alloys as biodegradable materials. *Frontiers of Materials Science in China* **2010**, *4* (2), 111−115.
(8) Liu, H. The effects of surface and biomolecules on magnesium degradation and mesenchymal stem cell adhesion. *J. Biomed. Mater. Res., Part A* **2011**, *99* (2), 249−260.
(9) Haude, M.; Ince, H.; Abizaid, A.; Toelg, R.; Lemos, P. A.; von Birgelen, C.; Christiansen, E. H.; Wijns, W.; Neumann, F.-J.; Kaiser, C.; et al. Safety and performance of the second-generation drug-eluting absorbable metal scaffold in patients with de-novo coronary artery lesions (BIOSOLVE-II): 6 month results of a prospective, multicentre, non-randomised, first-in-man trial. *Lancet* **2016**, *387* (10013), 31−39.
(10) Winzer, N.; Atrens, A.; Song, G.; Ghali, E.; Dietzel, W.; Kainer, K. U.; Hort, N.; Blawert, C. A critical review of the stress corrosion cracking (SCC) of magnesium alloys. *Adv. Eng. Mater.* **2005**, *7* (8), 659−693.
(11) Tian, Q.; Mendeza, J. A.; Rivera-Castaneda, L.; Mahmood, O.; Showalter, A.; Ang, E.; Kazmi, S.; Liu, H. Development of a novel loading device for studying magnesium degradation under compressive load for implant applications. *Materials Letters* **2018**, *217*, 27−32.
(12) Choudhary, L.; Raman, R. S.; Hofstetter, J.; Uggowitzer, P. J. In-vitro characterization of stress corrosion cracking of aluminium-free magnesium alloys for temporary bio-implant applications. *Materials Science & Engineering: C* **2014**, *42*, 629−636.
(13) Wong, H. M.; Yeung, K. W.; Lam, K. O.; Tam, V.; Chu, P. K.; Luk, K. D.; Cheung, K. M. A biodegradable polymer-based coating to control the performance of magnesium alloy orthopaedic implants. *Biomaterials* **2010**, *31* (8), 2084−2096.
(14) Jiang, W.; Tian, Q.; Vuong, T.; Shashaty, M.; Gopez, C.; Sanders, T.; Liu, H. Comparison study on four biodegradable polymer coatings for controlling magnesium degradation and human endothelial cell adhesion and spreading. *ACS Biomater. Sci. Eng.* **2017**, *3* (6), 936−950.
(15) Tian, Q.; Rivera-Castaneda, L.; Liu, H. Optimization of nano-hydroxyapatite/poly (lactic-co-glycolic acid) coatings on magnesium substrates using one-step electrophoretic deposition. *Mater. Lett.* **2017**, *186*, 12−16.
(16) Sebaa, M. A.; Dhillon, S.; Liu, H. Electrochemical deposition and evaluation of electrically conductive polymer coating on biodegradable magnesium implants for neural applications. *J. Mater. Sci.: Mater. Med.* **2013**, *24* (2), 307−316.
(17) Wang, J.; He, Y.; Maitz, M. F.; Collins, B.; Xiong, K.; Guo, L.; Yun, Y.; Wan, G.; Huang, N. A surface-eroding poly (1, 3-trimethylene carbonate) coating for fully biodegradable magnesium-based stent applications: toward better biofunction, biodegradation and biocompatibility. *Acta biomaterialia* **2013**, *9* (10), 8678−8689.
(18) Surmeneva, M. A.; Vladescu, A.; Cotrut, C. M.; Tyurin, A. I.; Pirozhkova, T. S.; Shuvarin, I. A.; Elkin, B.; Oehr, C.; Surmenev, R. A. Effect of parylene C coating on the antibiocorrosive and mechanical properties of different magnesium alloys. *Appl. Surf. Sci.* **2018**, *427*, 617−627.
(19) Caldwell, R.; Street, M. G.; Sharma, R.; Takmakov, P.; Baker, B.; Rieth, L. Characterization of Parylene-C degradation mechanisms: In vitro reactive accelerated aging model compared to multiyear in vivo implantation. *Biomaterials* **2020**, *232*, 119731.
(20) Sencadas, V.; Sadat, S.; Silva, D. M. Mechanical performance of elastomeric PGS scaffolds under dynamic conditions. *Journal of the mechanical behavior of biomedical materials* **2020**, *102*, 103474.
(21) Yang, X.; Wei, J.; Lei, D.; Liu, Y.; Wu, W. Appropriate density of PCL nano-fiber sheath promoted muscular remodeling of PGS/PCL grafts in arterial circulation. *Biomaterials* **2016**, *88*, 34−47.
(22) Zhang, X.; Jia, C.; Qiao, X.; Liu, T.; Sun, K. Porous poly (glycerol sebacate)(PGS) elastomer scaffolds for skin tissue engineering. *Polym. Test.* **2016**, *54*, 118−125.
(23) Sundback, C. A.; Shyu, J. Y.; Wang, Y.; Faquin, W. C.; Langer, R. S.; Vacanti, J. P.; Hadlock, T. A. Biocompatibility analysis of poly (glycerol sebacate) as a nerve guide material. *Biomaterials* **2005**, *26* (27), 5454−5464.
(24) Rothuizen, T. C.; Damanik, F. F.; Lavrijsen, T.; Visser, M. J.; Hamming, J. F.; Lalai, R. A.; Duijs, J. M.; van Zonneveld, A. J.; Hoefer, I. E.; van Blitterswijk, C. A.; et al. Development and evaluation of in vivo tissue engineered blood vessels in a porcine model. *Biomaterials* **2016**, *75*, 82−90.
(25) Bruggeman, J. P.; de Bruin, B.-J.; Bettinger, C. J.; Langer, R. Biodegradable poly (polyol sebacate) polymers. *Biomaterials* **2008**, *29* (36), 4726−4735.
(26) Chen, Q.-Z.; Liang, S.-L.; Wang, J.; Simon, G. P. Manipulation of mechanical compliance of elastomeric PGS by incorporation of halloysite nanotubes for soft tissue engineering applications. *Journal of the mechanical behavior of biomedical materials* **2011**, *4* (8), 1805−1818.
(27) Jiang, L.; Jiang, Y.; Stiadle, J.; Wang, X.; Wang, L.; Li, Q.; Shen, C.; Thibeault, S. L.; Turng, L.-S. Electrospun nanofibrous thermoplastic polyurethane/poly (glycerol sebacate) hybrid scaffolds for vocal fold tissue engineering applications. *Materials Science & Engineering: C* **2019**, *94*, 740−749.
(28) Zaky, S. H.; Hangadora, C. K.; Tudares, M. A.; Gao, J.; Jensen, A.; Wang, Y.; Sfeir, C.; Almarza, A. J. Poly (glycerol sebacate) elastomer supports osteogenic phenotype for bone engineering applications. *Biomedical Materials* **2014**, *9* (2), 025003.
(29) Kuroda, K.; Okido, M. Hydroxyapatite coating of titanium implants using hydroprocessing and evaluation of their osteoconductivity. *Bioinorganic chemistry and applications* **2012**, *2012*, 730693.
(30) Zhou, H.; Lee, J. Nanoscale hydroxyapatite particles for bone tissue engineering. *Acta biomaterialia* **2011**, *7* (7), 2769−2781.
(31) Webster, T. J.; Ergun, C.; Doremus, R. H.; Siegel, R. W.; Bizios, R. Enhanced functions of osteoblasts on nanophase ceramics. *Biomaterials* **2000**, *21* (17), 1803−1810.
(32) Rosenbalm, T. N.; Teruel, M.; Day, C. S.; Donati, G. L.; Morykwas, M.; Argenta, L.; Kuthirummal, N.; Levi-Polyachenko, N. Structural and mechanical characterization of bioresorbable, elastomeric nanocomposites from poly(glycerol sebacate)/nanohydroxyapatite for tissue transport applications. *J. Biomed Mater. Res. B Appl. Biomater* **2016**, *104* (7), 1366−73.
(33) Wang, Y.; Sun, N.; Zhang, Y.; Zhao, B.; Zhang, Z.; Zhou, X.; Zhou, Y.; Liu, H.; Zhang, Y.; Liu, J. Enhanced osteogenic proliferation and differentiation of human adipose-derived stem cells on a porous n-HA/PGS-M composite scaffold. *Sci. Rep.* **2019**, *9*, 7960.
(34) Wetteland, C. L.; Nguyen, N.-Y. T.; Liu, H. Concentration-dependent behaviors of bone marrow derived mesenchymal stem cells and infectious bacteria toward magnesium oxide nanoparticles. *Acta Biomater.* **2016**, *35*, 341−356.
(35) Carpenter, T. O.; DeLucia, M. C.; Zhang, J. H.; Bejnerowicz, G.; Tartamella, L.; Dziura, J.; Petersen, K. F.; Befroy, D.; Cohen, D. A randomized controlled study of effects of dietary magnesium oxide supplementation on bone mineral content in healthy girls. *Journal of Clinical Endocrinology & Metabolism* **2006**, *91* (12), 4866−4872.
(36) Nygren, H.; Chaudhry, M.; Gustafsson, S.; Kjeller, G.; Malmberg, P.; Johansson, K.-E. Increase of compact bone thickness in rat tibia after implanting MgO into the bone marrow cavity. *Journal of functional biomaterials* **2014**, *5* (3), 158−166.
(37) Sawai, J.; Kojima, H.; Igarashi, H.; Hashimoto, A.; Shoji, S.; Sawaki, T.; Hakoda, A.; Kawada, E.; Kokugan, T.; Shimizu, M.

https://doi.org/10.1021/acsami.4c13811
ACS Appl. Mater. Interfaces 2024, 16, 54716−54730

Antibacterial characteristics of magnesium oxide powder. *World J. Microbiol. Biotechnol.* **2000**, *16* (2), 187−194.
(38) Sawai, J. Quantitative evaluation of antibacterial activities of metallic oxide powders (ZnO, MgO and CaO) by conductimetric assay. *J. Microbiol. Methods* **2003**, *54* (2), 177−182.
(39) Nguyen, N.-Y.T.; Grelling, N.; Wetteland, C. L.; Rosario, R.; Liu, H. Antimicrobial Activities and Mechanisms of Magnesium Oxide Nanoparticles (nMgO) against Pathogenic Bacteria, Yeasts, and Biofilms. *Sci. Rep.* **2018**, *8*, 16260.
(40) Rosenbalm, T. N.; Teruel, M.; Day, C. S.; Donati, G. L.; Morykwas, M.; Argenta, L.; Kuthirummal, N.; Levi-Polyachenko, N. Structural and mechanical characterization of bioresorbable, elastomeric nanocomposites from poly (glycerol sebacate)/nanohydroxyapatite for tissue transport applications. *Journal of Biomedical Materials Research Part B: Applied Biomaterials* **2016**, *104* (7), 1366−1373.
(41) Ma, F.; Lu, X.; Wang, Z.; Sun, Z.; Zhang, F.; Zheng, Y. Nanocomposites of poly (L-lactide) and surface modified magnesia nanoparticles: fabrication, mechanical property and biodegradability. *J. Phys. Chem. Solids* **2011**, *72* (2), 111−116.
(42) Khandaker, M.; Li, Y.; Morris, T. Micro and nano MgO particles for the improvement of fracture toughness of bone-cement interfaces. *journal of biomechanics* **2013**, *46* (5), 1035−1039.
(43) Liu, H.; Webster, T. J. Mechanical properties of dispersed ceramic nanoparticles in polymer composites for orthopedic applications. *International journal of nanomedicine* **2010**, *5*, 299.
(44) Liu, H.; Webster, T. J. Enhanced biological and mechanical properties of well-dispersed nanophase ceramics in polymer composites: from 2D to 3D printed structures. *Materials Science & Engineering: C* **2011**, *31* (2), 77−89.
(45) Ostrowski, N.; Lee, B.; Enick, N.; Carlson, B.; Kunjukunju, S.; Roy, A.; Kumta, P. N. Corrosion protection and improved cytocompatibility of biodegradable polymeric layer-by-layer coatings on AZ31 magnesium alloys. *Acta Biomaterialia* **2013**, *9* (10), 8704−8713.
(46) Chen, Q.; Jin, L.; Cook, W. D.; Mohn, D.; Lagerqvist, E. L.; Elliott, D. A.; Haynes, J. M.; Boyd, N.; Stark, W. J.; Pouton, C. W.; et al. Elastomeric nanocomposites as cell delivery vehicles and cardiac support devices. *Soft Matter* **2010**, *6* (19), 4715−4726.
(47) Van Ooij, W.; Zhu, D.; Stacy, M.; Seth, A.; Mugada, T.; Gandhi, J.; Puomi, P. Corrosion protection properties of organofunctional silanes—an overview. *Tsinghua Science and technology* **2005**, *10* (6), 639−664.
(48) Jiang, W.; Zhang, C.; Tran, L.; Wang, S. G.; Hakim, A. D.; Liu, H. Engineering Nano-to-Micron-Patterned Polymer Coatings on Bioresorbable Magnesium for Controlling Human Endothelial Cell Adhesion and Morphology. *ACS Biomaterials Science & Engineering* **2020**, *6* (7), 3878−3898.
(49) Banerjee, P. C.; Raman, R. K. S. Electrochemical impedance spectroscopic investigation of the role of alkaline pre-treatment in corrosion resistance of a silane coating on magnesium alloy, ZE41. *Electrochim. Acta* **2011**, *56* (11), 3790−3798.
(50) Kunjukunju, S.; Roy, A.; Ramanathan, M.; Lee, B.; Candiello, J. E.; Kumta, P. N. A layer-by-layer approach to natural polymer-derived bioactive coatings on magnesium alloys. *Acta biomaterialia* **2013**, *9* (10), 8690−8703.
(51) Hänzi, A. C.; Gunde, P.; Schinhammer, M.; Uggowitzer, P. On the biodegradation performance of an Mg-Y-RE alloy with various surface conditions in simulated body fluid. *Acta biomaterialia* **2009**, *5* (1), 162−171.
(52) Janning, C.; Willbold, E.; Vogt, C.; Nellesen, J.; Meyer-Lindenberg, A.; Windhagen, H.; Thorey, F.; Witte, F. Magnesium hydroxide temporarily enhancing osteoblast activity and decreasing the osteoclast number in peri-implant bone remodelling. *Acta biomaterialia* **2010**, *6* (5), 1861−1868.
(53) Lock, J.; Nguyen, T. Y.; Liu, H. Nanophase hydroxyapatite and poly (lactide-co-glycolide) composites promote human mesenchymal stem cell adhesion and osteogenic differentiation in vitro. *J. Mater. Sci.: Mater. Med.* **2012**, *23* (10), 2543−2552.
(54) Wetteland, C. L.; Liu, H. Optical and biological properties of polymer-based nanocomposites with improved dispersion of ceramic nanoparticles. *J. Biomed Mater. Res. A* **2018**, *106* (10), 2692−2707.
(55) Johnson, I.; Akari, K.; Liu, H. Nanostructured hydroxyapatite/poly (lactic-co-glycolic acid) composite coating for controlling magnesium degradation in simulated body fluid. *Nanotechnology* **2013**, *24* (37), 375103.
(56) Cai, W.; Liu, L. Shape-memory effect of poly (glycerol-sebacate) elastomer. *Mater. Lett.* **2008**, *62* (14), 2171−2173.
(57) Zhou, W. Y.; Duan, B.; Wang, M.; Cheung, W. L. Crystallization kinetics of poly (l-lactide)/carbonated hydroxyapatite nanocomposite microspheres. *J. Appl. Polym. Sci.* **2009**, *113* (6), 4100−4115.
(58) Mobedi, H.; MIVEHCHI, H.; NEKOU, M. M.; ORAFAEI, H. Studying the degradation of poly (L-lactide) in presence of magnesium hydroxide. *Iranian Polymer Journal* **2006**, *15* (1), 31−39.
(59) Chen, X.; Yu, J.; Guo, S. Structure and properties of polypropylene composites filled with magnesium hydroxide. *J. Appl. Polym. Sci.* **2006**, *102* (5), 4943−4951.
(60) Fraschini, C.; Plesu, R.; Sarasua, J. R.; Prud'Homme, R. E. Cracking in polylactide spherulites. *J. Polym. Sci., Part B: Polym. Phys.* **2005**, *43* (22), 3308−3315.
(61) Sørensen, P. A.; Dam-Johansen, K.; Weinell, C.; Kiil, S. Cathodic delamination of seawater-immersed anticorrosive coatings: Mapping of parameters affecting the rate. *Prog. Org. Coat.* **2010**, *68* (4), 283−292.
(62) Lacombe, R. In *Adhesion Measurement Methods: Theory and Practice*; CRC Press, 2005; p 89−96.
(63) Liang, S.-L.; Cook, W. D.; Thouas, G. A.; Chen, Q.-Z. The mechanical characteristics and in vitro biocompatibility of poly (glycerol sebacate)-Bioglass® elastomeric composites. *Biomaterials* **2010**, *31* (33), 8516−8529.
(64) da Cunha, M. R.; Gushiken, V. O.; Issa, J. P. M.; Iatecola, A.; Pettian, M.; Santos, A. R., Jr Osteoconductive capacity of hydroxyapatite implanted into the skull of diabetics. *Journal of Craniofacial Surgery* **2011**, *22* (6), 2048−2052.
(65) Lin, L.; Chow, K. L.; Leng, Y. Study of hydroxyapatite osteoinductivity with an osteogenic differentiation of mesenchymal stem cells. *J. Biomed. Mater. Res., Part A* **2009**, *89* (2), 326−335.

https://doi.org/10.1021/acsami.4c13811
ACS Appl. Mater. Interfaces 2024, 16, 54716−54730